# Microstructure of Methylammonium Lead iodide Perovskite Thin Films: A Comprehensive Study of the Strain and Texture

Asma Medjahed, Tao Zhou, Juan Camilo Alvarez Quiceno, Pia Dally, Pascal Pochet, Tobias Schülli, David Djurado, Peter Reiss, Stéphanie Pouget

ThermoFisher SCIENTIFIC

Lithium-ion battery

# PowerUp webinars

## Analytical solutions for lithium-ion battery material analysis and testing

## PowerUp your battery material analysis - Join our educational webinars

Heading toward zero emission goals, lithium-ion battery are expected to generate an unprecedented demand for battery raw material in the upcoming decade. At the same time battery research, production, and quality control will need to keep up with the accelerated demand for electric storage capacities. Battery manufacturers must deliver consistently high quality throughout the entire battery value chain. Analysis and testing of batteries raw material and components requires therefore a variety of analytical methods that provide insights of quality and properties at various scales.

In this webinar session we will highlight the benefits of several analytical techniques and applications, as chromatography, mass spectrometry and electron microscopy, in battery material and structural analysis.

**Free education webinars**

**October 5 and 6, 2022 | 10:00 BST | 11:00 CEST**

**Part 1: Analysis of cathode materials**

**Part 2: Analysis of battery electrolytes**

No time for live session? Register anyway and get access to the on-demand recording after the live broadcast.

**Key learnings**

- Learn about analytical solutions for lithium-ion battery material and structural analysis
- Discover how IC, GC-MS, ICP-OES, and SEM support battery value chain from raw materials to recycling
- Get deeper insights based-on selected applications and performance examples

Learn more at **thermofisher.com/battery-webinars**

thermo scientific

ADVANCED ENERGY MATERIALS
www.advenergymat.de

# Microstructure of Methylammonium Lead iodide Perovskite Thin Films: A Comprehensive Study of the Strain and Texture

*Asma A. Medjahed, Tao Zhou, Juan Camilo Alvarez Quiceno, Pia Dally, Pascal Pochet, Tobias U. Schülli, David Djurado, Peter Reiss, and Stéphanie Pouget**

**Controlling the microstructure of hybrid halide perovskite thin films is essential for optimizing their performance in optoelectronic devices. It is well established that the strain state of the perovskite layer affects its stability. Likewise, the orientation of the perovskite lattice is a determining parameter as these materials have shown pronounced anisotropies in their physical and mechanical properties. In this work, the authors focus on the understanding of the mechanisms that govern the strain and texture observed in $MAPbI_3$ thin films deposited on various oxide substrates. A thorough study of the evolution of the strain of the perovskite layer upon cooling down to room temperature from the crystallization temperature (100 °C) shows an essentially relaxed behavior of the perovskite layers. This result contradicts the commonly accepted hypothesis according to which $MAPbI_3$ layers synthesized above ambient temperature are strained due to the large mismatch in the thermal expansion coefficients of the perovskite and its substrate. The texture in $MAPbI_3$ layers is investigated by means of synchrotron full-field diffraction X-ray microscopy. This technique allows the direct observation of the [hh0] and [00l]-oriented domains at the origin of the observed textures, demonstrating both their twin and ferroelastic nature. The stability of the different domain orientations is investigated by DFT calculations, illustrating the determining role of the chemical environment at the film-substrate interface. $PbI_2$- terminated surfaces are found to favor the [hh0] orientations while for MAI-terminated ones, both [hh0] and [00l] domains are equally stabilized. The different results constitute an important step of clarification and understanding from the perspective of controlling the microstructure of perovskite layers.**

## 1. Introduction

Once considered as a scientific curiosity, hybrid halide perovskite (HHP) materials have attracted a lot of interest over the past decade thanks to their application in optoelectronic devices and more particularly photovoltaics, with power conversion efficiencies (PCEs) readily comparable to those of crystalline silicon devices. Recently, microstructure engineering of the HHP layers, especially concerning the strain, has been at the forefront of device efficiency enhancement.[1] However, technological advances and the fundamental understanding of the processes at play during the perovskite thin film formation have evolved at different paces, and important questions are yet to be answered. Thus, apparent inconsistencies have been reported as halide perovskites systems exhibit either beneficial or detrimental effects of similar strain levels on different reports.[1–3] It is therefore essential to thoroughly understand the fundamentals of HHP layers strain intending to control it.[4–7] HHP are characterized by low values of their elastic constants,[8–10] more than one order of magnitude lower than the typical values of inorganic oxide perovskites,[11] which explains the high strain values that can be observed in thin films

A. A. Medjahed, D. Djurado, P. Reiss
University Grenoble Alpes
CEA
CNRS
IRIG
SyMMES
F-38054, Grenoble, France

The ORCID identification number(s) for the author(s) of this article can be found under https://doi.org/10.1002/aenm.202103627.



DOI: 10.1002/aenm.202103627

T. Zhou
Center for Nanoscale Materials
Argonne National Laboratory
Lemont, IL, USA

J. C. Alvarez Quiceno
Instituto de Fisica
Universidad de Antioquia UdeA
Calle 70 No 52-21, Medellin, Colombia

J. C. Alvarez Quiceno, P. Pochet, S. Pouget
University Grenoble Alpes
CEA
IRIG
MEM
F-38054, Grenoble, France
E-mail: stephanie.pouget@cea.fr

depending on the synthesis protocol.[12] Hybrid perovskites also exhibit large coefficients of thermal expansion (CTE). For instance, $FAPbI_3$ and $FASnI_3$ (FA = $CH(NH_2)_2$, formamidinium) show amongst the highest CTE values known for any 3D crystalline solids around room temperature (RT).[13–15] The large mismatch in CTE between the perovskite layer and the substrate, more than one order of magnitude, is commonly presented as determining the strain state of the layers when cooled down to RT after synthesis above 373 K,[3] although systematic and thorough investigations are lacking.

The texture is another important feature of the microstructure of hybrid metal halide perovskite layers. The perpendicular preferential orientations observed in $MAPbI_3$ layers are, in the majority of cases along the tetragonal [110] axis and occasionally along [001]. The co-existence of the two orientations (i.e., double texture) has also been reported in the literature but was rarely commented on.[16–19] The control of the perovskite lattice orientation is of paramount importance for applications since anisotropy in the physical properties of these materials is well-known.[10,20–22] In the case of $MAPbI_3$ thin films, identifying the origin of the texture requires rigorous consideration of the ferroelastic nature of the cubic-tetragonal transition which occurs around 330 K. The characteristic atomic arrangement of the perovskite structural family, in which a cation is located in the center of a cage formed by eight corner-sharing octahedra, is responsible for various and complex physical properties such as the multiferroism, observed in several perovskite compounds. In the case of $MAPbI_3$, studies using local probes such as transmission electron microscopy (TEM), scanning electron microscopy (SEM), atomic force microscopy (AFM), and piezoresponse force microscopy (PFM), have demonstrated the presence of an intragrain stripped, needle-like structure in thin layers.[23–26] Using TEM and SAED (Selected Area Electron Diffraction), Rothmann et al. demonstrated that these striped structures in the layer arise from the existence of {112} twin domains.[23] The existence of these domains at room temperature has been explained by the phase transition experienced by the material after its synthesis. $MAPbI_3$ thin layers are usually obtained by thermal annealing at 373 K, the temperature at which the perovskite crystalline phase adopts a cubic $Pm\bar{3}m$ structure. As the sample is cooled down, it experiences a structural phase transition around 330 K[27] to adopt the tetragonal structure I4/mcm, stable at RT. At this phase transition, the loss of the cubic threefold axis generates three possibilities for the orientation of the tetragonal *c*-axis, leading to the formation of twin domains. Moreover, the $Pm\bar{3}m$–I4/mcm phase transition is expected to be ferroelastic:[28] similar to what is observed with ferroelectric materials for which domains can be modulated using an electrical field, ferroelastic domains are sensitive to the application of external mechanical stress. By bending the sample with different radii and directions, Strelcov et al. showed the ferroelastic character of the domains observed in $MAPbI_3$ films, which were switched by the stress generated by the bending deformation.[29] However, in a more recent study, twin domains have also been observed in $MAPbI_3$ samples which have not experienced the cubic-tetragonal transition,[30] indicating the potential existence of intrinsic or "static" twin domains in the thin films in addition to the ferroelastic ones. The observed textures of the $MAPbI_3$ layers depend, at least in part, on the presence and behavior of such domains.

This study focuses first of all on the understanding of the mechanisms at the origin of the strain and texture observed in $MAPbI_3$ thin layers, the control of both allowing the optimization of the optoelectronic properties, device performances and stability.[31,32] We do so by systematically comparing the strain evolution and preferential domain orientations on $MAPbI_3$ layers prepared with and without chlorine, on various types of inorganic oxide substrates. Despite being present in trace amounts in the final material,[33,34] the use of controlled amount of chlorine in the precursors solution is known to be beneficial for photovoltaic applications of the material. In addition to improving for instance the charge carrier diffusion length,[35,36] it has been shown to strongly enhance the tendency of the perovskite lattice to grow with preferential orientations.[37] The evolution of the strain state of the perovskite films prepared in the presence of chlorine or not is carefully investigated by means of in situ laboratory XRD experiments across the cubic-tetragonal phase transition. As the layer is cooled down, the determined values of the lattice parameters evidence a mainly relaxed state of the film, despite the perovskite/substrate CTE mismatch. Below the cubic to tetragonal phase transition, $MAPbI_3$ prepared with Cl showed predominantly [hh0] oriented domains and occasionally [00l] oriented ones. With synchrotron full-field diffraction X-ray microscopy, we confirmed that the [00l] oriented domains are in fact twins to the [hh0] oriented domains as they were spatially correlated. Additionally, we were able to convert the [00l] domains into [hh0] through X-ray photon induced chemical stress, thus proving their ferroelastic character. Finally, we were able to explain the scarcity of the [00l] domains through DFT calculations. Depending on the chemical nature of interface termination, the formation energy can be as much as 50 meV lower for the [hh0] domains than for the [00l] ones.

## 2. Strain in MAPbI3 Thin Layers

In order to carry out a comprehensive study of the strain found in $MAPbI_3$ thin films, we investigated two types of layers, obtained through protocols largely used in the literature.[36,38] Hereinafter for the sake of clarity, thin layers prepared without chlorine will be labelled $MAPbI_3$ whereas those obtained with chlorine will be referred to as $MAPbI_3$(Cl). The precursor solutions were deposited on various substrates (glass/ITO/$SnO_2$, glass/ITO, glass/ITO/$TiO_2$) prepared as indicated in the experimental section.

P. Dally
Institut Lavoisier de Versailles (ILV)
Univ. Versailles Saint-Quentin-en-Yvelines
Univ. Paris-Saclay
CNRS
F-78035, Versailles, France
P. Dally
IPVF
F-91120, Palaiseau, France
T. U. Schülli
The European Synchrotron ESRF
BP 220, Grenoble 38043 Cedex 9, Grenoble, France

The obtained chlorine-free $MAPbI_3$ thin films deposited on glass/ITO/$SnO_2$ are polycrystalline, in agreement with previous reports.[37] The pattern is coherent with tetragonal I4/mcm symmetry at RT and out-of-plane lattice parameters were extracted by LeBail refinement as $a_{perp} = 8.872(2)$ Å and $c_{perp} = 12.658(4)$ Å. On the other hand, $MAPbI_3$(Cl) display a preferential orientation along [hh0] tetragonal direction, as expected when using chlorine in the precursor solution[37] and the out-of-plane lattice parameter was calculated from the position of the (hh0) peaks as $a_{perp} = 8.868(4)$ Å. To evaluate the strain in these layers, bulk $MAPbI_3$ powder was prepared and used as an unstrained reference. The RT diffractogram of the powder and its profile refinement is presented in Figure S1, Supporting Information; lattice parameters of $a = 8.876(2)$ Å and $c = 12.667(2)$ Å were refined, in good agreement with previously reported values.[27] We calculated the linear CTE of the powder in the cubic phase at $T = 80$ °C as $\alpha_L^{cub} = 3.8(2) \times 10^{-5} K^{-1}$, which is also in good agreement with values reported in the literature for $MAPbI_3$ thin films[39] or single crystals;[40] it is significantly larger, by one order of magnitude, than the linear CTE values of glass or ITO ($\alpha_L$ between $4 \times 10^{-6}$ and $8 \times 10^{-6}$ $K^{-1}$ [3]). This large CTE difference is highlighted in Figure S2, Supporting Information. At RT, the out-of-plane lattice parameters for $MAPbI_3$(Cl) and $MAPbI_3$ layers reveal weak out-of-plane compressive strain levels, between –0.09 and –0.04% (strain $\varepsilon$ calculated as follows $\varepsilon = \frac{a_{sample} - a_{bulk}}{a_{bulk}}$).

Attention has lately been dedicated to strain engineering in hybrid halide perovskite, as it is believed that the presence of strain weakens the material and decreases the performance of the devices. Since Zhao et al. work,[3] it is commonly considered that when the layer is synthesized around 100 °C, it is subjected, during cooling, to tensile in-plane stress due to the large mismatch of CTE between the perovskite and substrates such as glass/ITO and glass/ITO/$SnO_2$. In order to deeply investigate this process, we followed by in situ XRD the evolution of the strain state in our perovskite layers from the crystallization of $MAPbI_3$ and $MAPbI_3$(Cl) at 100 °C down to RT.

After spin-coating the precursor solution on a glass/ITO substrate in a glove box, the as-cast thin layer is transported in a sealed box to the diffractometer equipped with an oven pre-heated at 100 °C, and the sample is kept under inert atmosphere. The crystallization of the perovskite is thereafter monitored through repetitive $\theta/2\theta$ scans. Once the crystallization is completed, the temperature of the sample is lowered in steps of 10 °C, and $\theta/2\theta$ diffractograms are measured for each temperature between 100 and 30 °C. The evolution of the out-of-plane lattice parameter of the perovskite during the first cooling ramp experienced by the layer, immediately after the crystallization is thus carefully followed. The results obtained for $MAPbI_3$ and $MAPbI_3$(Cl) thin layers are presented in **Figure 1**. The black hollow symbols point to the temperature-dependent lattice parameters of the bulk powder reference.

Figure 1 also shows the in-plane lattice parameter values of the $MAPbI_3$ and $MAPbI_3$(Cl) thin layers. Since they could not be measured with sufficient precision, the in-plane parameters were determined, in the cubic phase, from the out-of-plane strain values by applying Hooke's law in the case of biaxial in-plane stress. Details of the calculation are provided in Supplementary Materials. In the temperature range from 100 °C to 60 °C, above the cubic-tetragonal phase transition, both $MAPbI_3$ and $MAPbI_3$(Cl) layers evidence a mainly relaxed behavior, with their out-of-plane and in-plane lattice parameters being very close to those of the bulk material.

The same experiment was performed on thin layers deposited on various oxide substrates (glass/ITO/$SnO_2$ and glass/FTO/$TiO_2$ in addition to the above-presented glass/ITO substrates, see Figure S3, Supporting Information), leading to the same results: the layers are mainly relaxed, with a thermal contraction following closely the one observed on bulk material. Moreover, $MAPbI_3$(Cl) layers prepared in slightly different conditions were studied similarly, leading to the same thermal behavior (more details in the Supplementary Materials and Figure S4, Supporting Information). Moreover, the temperature-dependent in-plane and out-of-plane strains (Figure S5a, Supporting Information) and deduced bi-axial stress (Figure S5b, Supporting

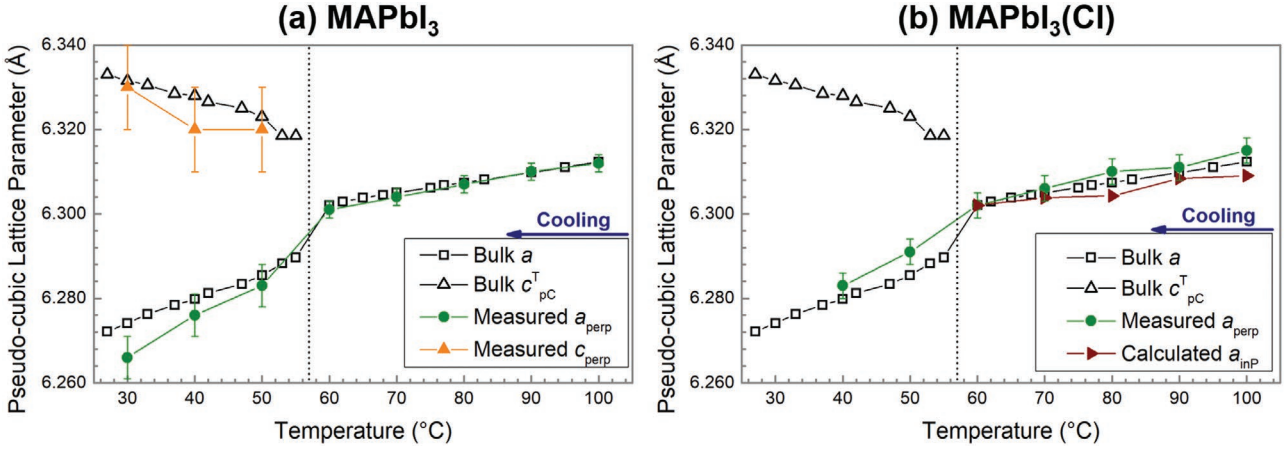


**Figure 1.** Evolution of the measured out-of-plane and calculated in-plane lattice parameters during controlled cooling down from 100 °C to RT of $MAPbI_3$ a) and $MAPbI_3$(Cl) b) thin layers deposited on glass/ITO. For $MAPbI_3$(Cl) (b), the sample displays a unique [hh0] texture in the tetragonal phase, hence only out-of-plane *a* lattice parameter could be extracted from $\theta/2\theta$ scans. The open symbols display the lattice parameters of the unstrained, bulk reference sample and the dotted lines indicate the cubic-tetragonal phase transition temperature in the bulk material (57 °C).

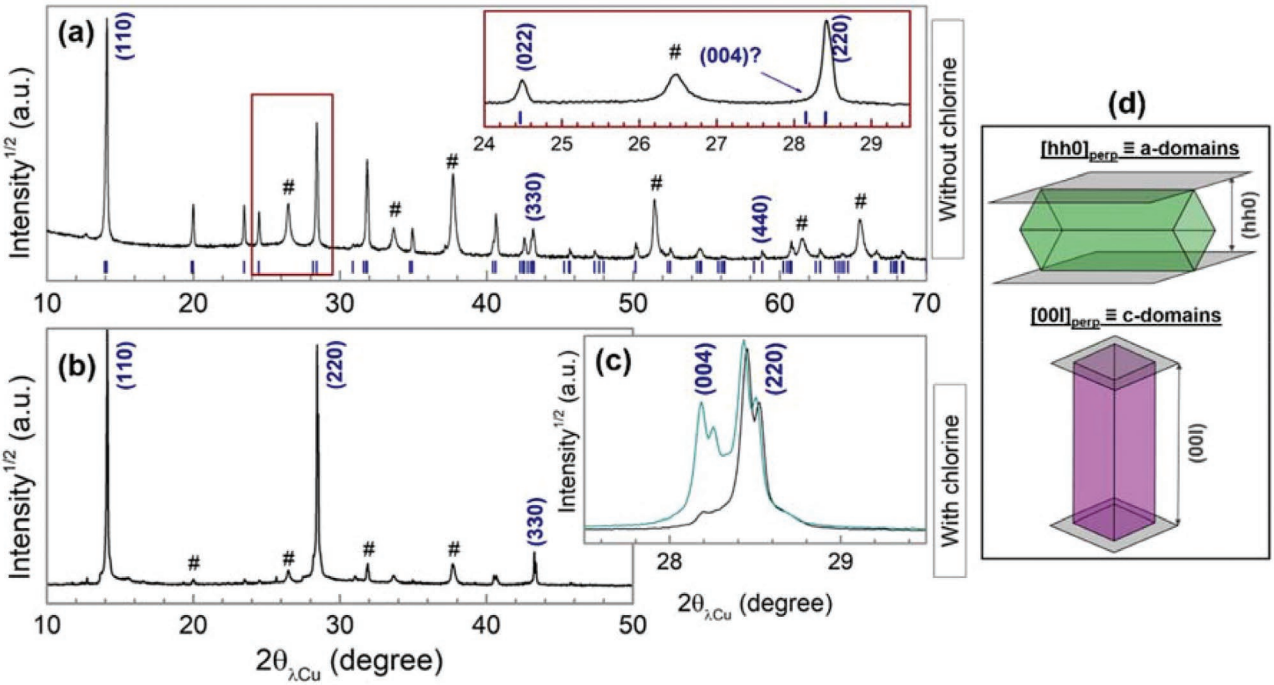


**Figure 2.** Representative $\theta/2\theta$ XRD patterns of the different thin layers studied. a) Polycrystalline $MAPbI_3$ layer (no Cl in the precursors). The blue dashes point to the expected peak positions for the tetragonal I4/mcm $MAPbI_3$ thin layer, obtained from profile refinement of the pattern with $a = 8.872(1)$ Å and $c = 12.658(3)$ Å. An enlarged view of the pattern in the range $2\theta$ from 22 to 29 ° is shown in the inset, highlighting the good agreement between the calculated and observed diffraction lines, as well as the absence of the (004) Bragg peak at its expected position. b) Typical $MAPbI_3$(Cl) layer with a [hh0] texture. c) Partial $\theta/2\theta$ patterns for two $MAPbI_3$(Cl) samples with two different textures: [hh0] only (black) and [00l]/[hh0] double texture (light blue). In all patterns, the #symbol denotes the position of the Bragg peaks of the FTO/$TiO_2$ substrate. d) Schematic representation of *a*- and *c*-domains. The direction probed when performing $\theta/2\theta$ measurements is perpendicular to the grey planes.

Information) were calculated, showing low and mainly constant values over the probed temperature range.

Our results evidence that our perovskite layers deposited on transparent conducting oxides (TCO) following commonly used protocols have a mainly free thermal behavior and are mainly relaxed. They show, at the very least, that the commonly accepted hypothesis according to which the large CTE mismatch between the HHP and the substrate systematically induces strain in the perovskite film upon cooling down[3] should be questioned. Following this hypothesis, cooling down a perovskite layer deposited on glass/ITO from 100 °C to RT should lead to an in-plane strain of $\varepsilon = \Delta\alpha\,(T - 100) = 10^{-3}$ at RT, and our experiments (Figure 1) and calculations (Figure S5, Supporting Information) clearly prove that it is not the case. The free thermal contraction was observed on various types of perovskite layers ($MAPbI_3$ and $MAPbI_3$(Cl)), deposited on various substrates.

These results lead us to further question the fact of considering the CTE mismatch as the main relevant parameter determining the film strain state. Several processes can be considered. The first one could be, considering the variety of possible chemical reactions at the substrate/perovskite interface,[36] the existence of weak coupling (pseudo-van der Waals type) between the perovskite and the oxide substrate. However, it seems more likely in the case of MAI-terminated interfaces rather than in the case of $PbI_2$ ones. In the hypothesis of strong coupling between the film and the substrate (e.g., covalent type), the presence of dislocations beyond a critical thickness (as defined by Mattews and Blackslee in the case of epitaxial layers[41]) can lead to a relaxed film. Worth is noticing that in the case of soft materials such as $MAPbI_3$ such a relaxation process is rather unlikely as the perovskite lattice can accommodate a high level of strain[1,12]. Grain boundaries might play a key role in the strain relaxation,[42] more particularly combined with the high ion mobility observed in this material which has been shown to favor the mitigation of lattice defects.[43] Further investigations are required to clearly identify the mechanisms governing the strain behavior in $MAPbI_3$ layers.

## 3. Texture in $MAPbI_3$ Thin Layers

The second issue addressed in this work concerns the texture of the different $MAPbI_3$ thin layers. A close inspection of the $\theta/2\theta$ XRD patterns obtained with $MAPbI_3$ layers reveals the absence of the (00l) diffraction lines, as can be seen in the enlarged view of the diffraction pattern in **Figure 2**a), in which an arrow points at the expected position for the (004) peak. Since a $\theta/2\theta$ measurement only probes the direction normal to the surface plane, we performed complementary in-plane measurements on the same $MAPbI_3$ thin layer. The result, shown in Figure S8, Supporting Information, confirms the presence of (00l) peaks in this configuration. This feature was systematically observed on various substrates (glass/FTO/$TiO_2$,

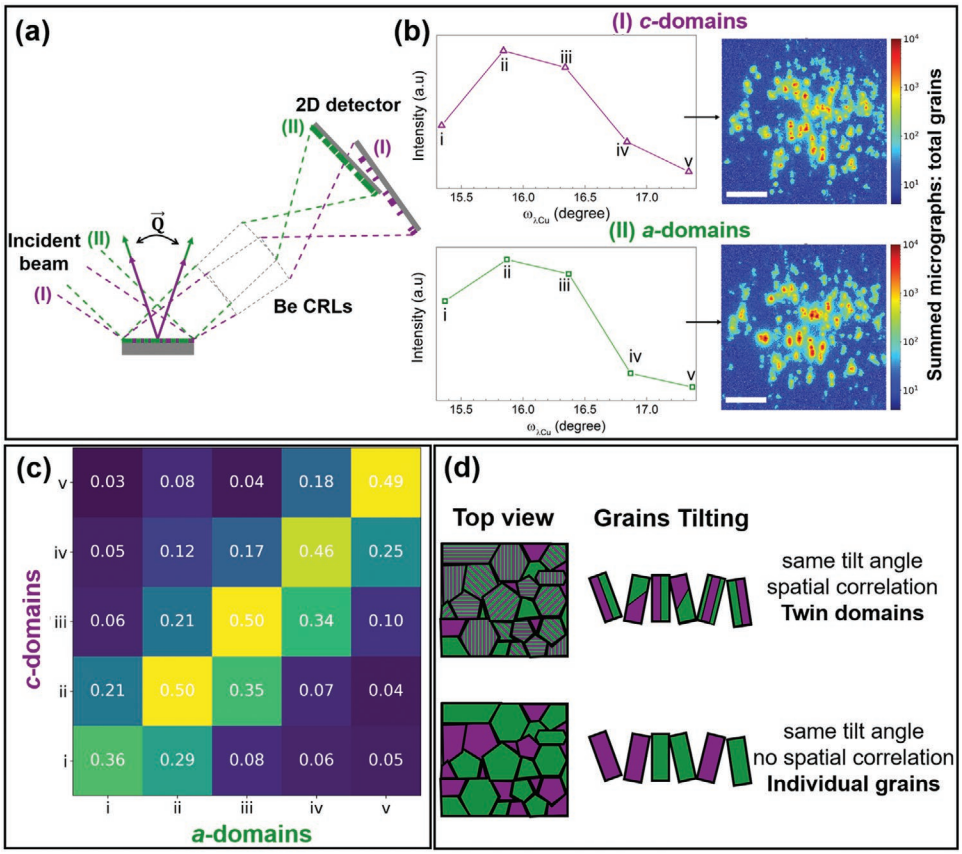


**Figure 3.** Rocking curve measurements with FFDXM at ESRF. Measurement configuration a), obtained rocking curves for both *a*- and *c*-domains and resulting summed micrographs showing all *a* and *c*-domains b). c) Correlation map of *a* and *c*-domains obtained from rocking curve measurements. d) Schematic of the presence or absence of spatial and tilting correlation in the grains, illustrating the results of the correlation map; purple and green colors respectively correspond to *c*- and *a*-domains.

glass/ITO/$SnO_2$, glass/ITO) and across different synthetic protocols (fast crystallization[44] or solvent engineering[45] methods). Concerning $MAPbI_3$(Cl) films, they mainly present a unique texture along [hh0], with a mosaicity of ≈5 ° (Figure S7, Supporting Information). However, some layers display a double texture [hh0]/[00l] (Figure 2b,c). The presence of this second orientation has already been reported but rarely commented on.[16–19] For tetragonal (00l) diffraction peaks to appear on $\theta/2\theta$ scans, the *c*-axis needs to be perpendicular to the surface plane. The fact that these peaks are not observed in $MAPbI_3$ and rarely on $MAPbI_3$(Cl) indicates that this orientation of the crystallites is not energetically favorable. This observation is consistent with a previous report of Rothmann et al. using TEM and SAED,[23] where most of the perovskite grains presented striped domains, identified as two distinct twins, both characterized by their *c*-axis lying in the layer plane. The study of the texture in our different HHP layers was thus driven by two problematics: understanding the nature of the double orientation which can arise in $MAPbI_3$(Cl) and determining the origin of the preferred orientation characterized by the tetragonal *c*-axis rarely pointing perpendicularly to the sample's plane.

To investigate the nature of the double [hh0]/[00l] texture, synchrotron Full-Field Diffraction X-ray Microscopy (FFDXM) was used. Synchrotron-based experiments previously proved to be highly beneficial and informative tools to study the properties of halide perovskites,[46] and FFDXM is a powerful technique allowing direct mapping of crystalline domains. Details about the unique FFDXM experimental setup on the ID01 beamline at the European Synchrotron Radiation Facility (ESRF) are found in the experimental section.[47–49] As shown in **Figure 3**a), the sample is illuminated by a quasi-parallel beam. A dark field image is formed on the 2D detector by a set of beryllium compound refractive lenses (Be CRLs) serving as the objective optics. The darkfield selectivity of the FFDXM can be used, for instance, to image separately the [hh0] and the [00l] domains. This is achieved by tuning the incident and diffraction angle to their respective $\theta$ and $2\theta$ values.

For simplicity, we shall refer hereinafter to the [hh0]-oriented crystallites as *a*-domains and to the [00l]-oriented ones as *c*-domains, as illustrated in Figure 2.d). A $MAPbI_3$(Cl) thin layer is deposited on monocrystalline rutile $TiO_2$. We previously demonstrated texture enhancement of perovskite layers using this type of substrate,[37] with a mosaicity reduced down to ≈1–2 ° (figure S10b). Investigating a sample presenting the double [hh0]/[00l] texture (figure S10, Supporting Information), a 5-point rocking curve was performed around the (004) and (220) reflections, respectively, to image domains of different

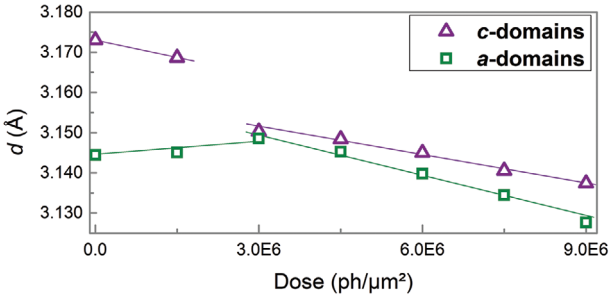


**Figure 4.** Evolution of the inter-reticular distance of initially *a*- and *c*-domains when exposed to increasing X-ray beam dose.

tilting angles from the normal. The number of points on the rocking curve was limited to minimize sample damage due to exposure to the X-ray beam. The integrated dark field intensities of the rocking curves are shown in Figure 3b). The right part of this figure shows the resulting two micrographs obtained when stacking the 5 micrographs measured on each type of domain. We have calculated the cross-correlation between the dark field images of the *a*- and *c*-domains, resulting in a (5 × 5) correlation map displayed in Figure 3c). Details about the procedure to extract this table are given in Supplementary Materials.

The result shows strong correlation along and near the diagonal, and almost no correlation away from it. This indicates that *a*- and *c*-domains with the same tilting angles are found on top of each other (figure 3b), and are thus twin domains originating from the same cubic grain at high temperature. We note that if the *c*-domains were randomly distributed, the correlation map would have ≈0 everywhere. In fact, the ≈0.5 spatial correlation on the diagonal indicates that at least 50% of the observed grains are twinned, which is an impressive amount considering the scarcity of the *c*-domains.

As illustrated in Figure S13, Supporting Information and mentioned in the work of Kennard et al. work,[2] *a*– and *c*-domains follow the same twin law as the one identified by TEM.[23] While previous studies attributed the double [hh0]/[00l] texture to twin domains solely based on classical XRD measurements which average the signal over a large area on the sample and do not allow to probe the spatial correlation of the different domains,[2,12] we provide here a direct proof of the twin nature of these domains through local observations.

Having demonstrated that the observation of the double texture [hh0]/[00l] is related to the presence of twin domains in the perovskite layer, we now address the question of the nature of these twins, whether they are ferroelastic or not since both cases have been previously reported.[29,30] A specificity of ferroelastic domains is the switching between different twin orientations under applied mechanical stress.[50] In the following, we select single domain *a*- and *c*-grains (without twins) and follow their behavior when exposed to the X-ray beam.

Exposure to intense X-rays typically accelerates the decomposition of hybrid perovskites into Pb(0), $I_2$, and organic degradation products.[51,52] This decomposition is characterized by a general but not immediate decrease of the overall intensity as well as broadening of the perovskite Bragg peaks. Stuckelberger et al. have shown that the interaction of $MAPbI_3$ with 8 keV photons induces ionic diffusion,[53] which is most probably at the origin of the observed degradation upon increasing the radiation dose. The same ionic diffusion can be reasonably hypothesized to be at the origin of the strain observed in the perovskite before its decomposition. In this study, we exploit this effect to test the ferroelastic nature of *a*- and *c*-domains. We note that the *d*-spacing we measured is not affected by the perovskite decomposition products as they do not diffract at these angles. Instead, we are measuring the remaining perovskite strained by the beam induced ionic diffusion.

**Figure 4** shows the evolution of the *d*-spacing under beam exposure. We were able to separately measure the *d*-spacing of the two types of domains thanks to the dark field sensitivity of FFDXM; the details of the data treatment are given in the Supplementary Materials. The right-hand side of the figure shows the decomposition induced strain which scales linearly with the fluence, at about $5 \times 10^{-4}$ per 1 million photons per μm². The same strain per fluence was observed on the *c*-domains at the beginning of the beam exposure (left-hand side). Figure S12, Supporting Information, displays the evolution of *a*-domains peak area under a synchrotron X-ray beam, showing that the beam-induced degradation starts for doses around $4 \times 10^6$ photons per μm². A sudden jump in *c*-domains *d*-spacing was observed at $3 \times 10^6$ photons per um². After this jump, the out-of-plane lattice parameter of the *c*-domains matches that of the *a*-domains, indicating a transition has taken place that switched the former into the latter. The strain threshold for this transition is about −0.13%. Concerning the *a*-domains, the *d*-spacing is mainly constant up to $3 \times 10^6$ photons per μm² before the appearance of compressive strain. Statistical analysis performed on different regions of the sample proved the reproducibility of this behavior. These observations strongly suggest a switching of *c*-domains into *a*-domains, most probably caused by the X-ray exposure induced chemical strain, illustrating the ferroelastic nature of these domains.

Finally, we address the question of the origin of the textures observed in $MAPbI_3$ and $MAPbI_3$(Cl) thin films. As previously mentioned, all $MAPbI_3$ and most $MAPbI_3$(Cl) layers present a preferential orientation of the tetragonal *c*-axis in the sample's plane, indicating that *c*-domains are energetically disfavored. We aim at identifying the origin of the raise of degeneracy in the stability of the different twin domains. One hypothesis could be the strain. However, from the in situ XRD study of different layers upon cooling down presented in the previous section (Figure 1), no correlation could be established between the strain state of the perovskite layer before the cubic-tetragonal structural phase transition and the texture observed in the tetragonal phase. To identify the possible origin of the texture observed in the $MAPbI_3$ layers, we conducted a numerical study to evaluate the relative stability of *a*- and *c*-domains for different possible terminated surfaces. The energy at zero Kelvin was calculated for nine different configurations: for each of the three orientations ($[\bar{h}h0]$ and [hh0] *a*-domains and [00l] *c*-domains) two types of surfaces are considered, MAI- or $PbI_2$-terminated. The calculations were done using Density Functional Theory using the PBE functional[54] and the VASP code.[55] In **Figure 5**, we present the case of a doubly $PbI_2$-terminated slab, the two types of boxes containing 6 and 12 MA molecules respectively;

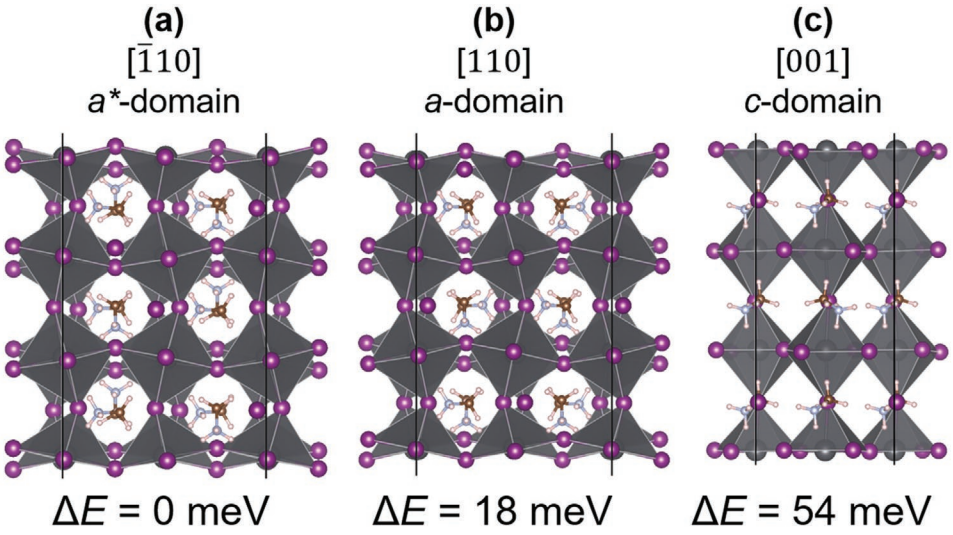


**Figure 5.** The three $PbI_2$-terminated configurations considered in the DFT calculations corresponding to a) [$\bar{1}$10] b) [110] and c) [001] orientations. Both side and top views are represented. Pb, I, C, N, and H atoms are dark-grey, purple, brown, light blue, and white spheres respectively. The normalized total energy, as well as the relative energy to the ground state, are reported for each configuration.

the total energy needs to be normalized by the number of MA molecules to allow comparison.

The result shows that the energy of both types of *a*-domains are very close, the difference (18 meV per MA) being lower than the thermal energy at RT (26 meV). Both variants can thus be expected to be present in $MAPbI_3$ layers, as confirmed by Rothmann et al.[23] The most striking result concerns the *c*-domains orientation which is predicted to be the less thermodynamically stable one by more than 50 meV when compared to the ground state of the series. Interestingly, if we consider mixed terminated surfaces as shown in Figure S14, Supporting Information, we note that the relative stability is reverted, the *c*-domain orientation being now the ground state for these stoichiometric configurations as also expected for 2D perovskites grown in MA-rich conditions. These results point to the role of the local chemical equilibrium close to the interface with the substrate. In the case of Pb-rich conditions, we predict that *a*-domains will be favored while the reverse is true for stoichiometric or MA-rich conditions. The perovskite-substrate interaction has been at the center of numerous studies generally applying substrate surface functionalization to improve the morphology and optoelectronic properties of the perovskite layer.[36] The DFT calculation results presented here evidence that the chemical environment at the interface with the substrate plays a key role in the origin of the preferential orientation of the domains, shedding new light on the complex perovskite-substrate interaction mechanisms.

## 4. Conclusion

This study focuses on the microstructure, namely texture and strain, in hybrid halide perovskite $MAPbI_3$ and $MAPbI_3$(Cl) thin films. Utilizing in-situ XRD experiments performed on perovskite layers deposited on different TCO substrates, we showed that $MAPbI_3$ contracts mainly freely on the substrate when it is cooled down to RT after synthesis and annealing at 100 °C. Contrary to what has been commonly reported, our results prove that there is no direct correlation between the existence of a large CTE mismatch between the perovskite material and the substrate and the presence of strain in $MAPbI_3$ layer. Synchrotron full-field diffraction X-ray microscopy was used to investigate the peculiar [hh0]/[00l] double texture sometimes observed in $MAPbI_3$(Cl) layers instead of the more common [hh0] one. The high tilt and space resolutions of the FFDXM technique provide clear evidence that the observed textures are related to the presence of twin domains. The ferroelastic nature of these twins is asserted by the observation of the switching of [00l] domains into [hh0] ones under X-ray beam exposure. Concerning the origin of the texture, the results of our DFT-based numerical study evidence the correlation between the composition of the first perovskite plane at the interface with the substrate (MAI or $PbI_2$ type) and the stability of the different twin orientations.

We believe that this comprehensive study constitutes an important contribution regarding the complex but crucial problem of the control of the microstructure of HHP layers. The scope of our results goes beyond the single case of $MAPbI_3$ as strain and texture control is required for a large number of HHP based applications. We thus believe that this work paves the way to reach better control of the microstructure of halide perovskite thin films, which is essential in the aim of improving the performance of HHP based solar cells and other types of devices.

## 5. Experimental Section

*$MAPbI_3$ Thin Film Deposition*: All substrates (glass/ITO, glass/FTO and single-crystalline rutile $TiO_2$) were pre-cleaned in an ultrasonic bath, subsequently, in deionized water, ethanol, and acetone for 10 min each, followed by drying under $N_2$ flow and ultra-violet ozone cleaning for 45 min at RT. Part of the precleaned ITO/glass substrates were used to deposit a ≈60 nm $SnO_2$ thin layer prepared by spin-coating an aqueous

colloidal solution of nanoparticles (Alpha Aesar), followed by drying at 80 °C for 1 min and annealing at 220 °C for 20 min. $TiO_2$ layers were also deposited on precleaned glass/FTO substrates by spin-coating a precursor solution of 1 ml of ethanol, 76 µl of acetyl acetonate and 130 µl of Ti(IV) isopropoxide. 60 µl of the solution was spin-coated on $1 \times 1$ cm substrates at 3000 rpm for 30 s. The substrates were afterwards annealed in the oven at 500 °C for 30 min.

$MAPbI_3$ thin layers were prepared from a precursor solution of equimolar MAI (Dyesol, GreatCell Solar) and $PbI_2$ (TCI, 99.99%) dissolved in anhydrous DMF (Sigma-Aldrich) to form a 0.8 M solution. $MAPbI_3$(Cl) layers were obtained using a precursor solution containing MAI and $PbCl_2$ (Sigma-Aldrich, 99.99%) in a 3:1 molar ratio dissolved in anhydrous DMF to respect the stoichiometry of the final compound. The 0.8 M precursors solution was stirred at RT until the full dissolution of the precursors. All solutions were spin-coated using the same protocol: 5000 rpm for 30 s with 75 µl of the anti-solvent chlorobenzene being dripped after 7 s. Subsequent annealing at 100 °C was performed for 10 min and 30 min for $MAPbI_3$ and $MAPbI_3$(Cl) thin layers, respectively.

For $MAPbI_3$(Cl) thin layers with a higher precursor solution concentration, the 1.6 M solution was obtained again from MAI and $PbCl_2$ in a 3:1 ratio in anhydrous DMF. The solution was stirred at 70 °C until the complete dissolution of the powders. The same spin-coating protocol as previously detailed was used and annealing was performed at 110 °C for 35 min.

*Laboratory XRD*: In-situ XRD measurements of $MAPbI_3$(Cl) thin films were carried out using a Rigaku Smartlab X-ray diffractometer equipped with a copper rotating anode, a goniometer with a $\theta/\theta$ configuration (horizontal sample), and a DHS 1100 Anton Paar domed hot stage. The sample was kept under a controlled atmosphere ($N_2$ flux).

Temperature-dependent XRD measurement of powder sample was performed on a Bruker D8 advanced diffractometer, equipped with a copper anode and a 1D LynxEye detector. It was configured in Bragg-Brentano geometry, with variable divergence slit on the primary beam path and a set of anti-scattering slits positioned before and after the sample. The diffractometer was equipped with an Anton Paar temperature chamber TTK600.

*FFDXM at ID01 (ESRF)*: Full-field diffraction X-ray microscopy experiments were carried out on the ID01 beamline at the European synchrotron (ESRF).[47–49] The photon energy was 8 keV. A set of Beryllium Compound Refractive Lenses (CRLs) was put about 100 mm downstream of the sample, in the path of the diffracted beam. The Field of View was about $230 \times 230$ µm$^2$. The dark field image was formed on an Andor sCMOS camera (6.5 µm pixel size) behind 15 µm of Gadox scintillator, also in the path of the diffracted beam. At 6.5 m lenses to detector distance, the magnification ratio is about 65× which results in an effective pixel size of 100 nm. The actual spatial resolution is about 150 nm due to imperfections in the lenses. Both the lenses and the detector can rotate freely in the horizontal scattering plane, to image diffracted photons at specific $2\theta$ angles. For a rocking scan, the lenses and detectors are fixed, while only the sample rotates.

*DFT Calculations*: The theoretical study was carried out by using first-principles calculations based on DFT. The exchange–correlation potential was treated within the generalized gradient approximation (GGA) with the PBEsol parametrization.[54] The projected augmented wave (PAW) method[56] was used to solve the Kohn–Sham equations as implemented in the Vienna ab Initio Simulation Package (VASP)[55] with a kinetic energy cutoff for the plane-wave expansion of 910 eV. The surfaces were cleaved from the bulk tetragonal $MAPbI_3$ phase where the crystal lattice parameters were first optimized ($a$ = 8.775Å and $c$ = 12.668Å). The optimization of atomic positions was performed using a conjugate gradient algorithm until the Hellmann–Feynman forces reached the threshold of $0.1 \times 10^{-3}$ eV Å$^{-1}$. A vacuum of at least 15 Å was employed to avoid undesired interactions between periodic layers. The Brillouin zone was sampled with a $6 \times 6 \times 1$ and $4 \times 4 \times 1$ $k$-point meshes for the <001> and the <110> slab configuration respectively which leads to similar ≈0.02 $k$-points Å$^{-1}$ sampling on all the slabs.

## Supporting Information

Supporting Information is available from the Wiley Online Library or from the author.

## Acknowledgements

The authors acknowledge the French Research Agency ANR for financial support (grants SuperSansPlomb ANR-15-CE05-0023-01 and PERSIL ANR-16-CE05-0019-02) and the LABEX Lanef in Grenoble (ANR-10-LABX-51-01) for its support with mutualized instrumentation. Dr. Mathilde Bouchard is thanked for thin layers fabrication. The European Synchrotron is thanked for beamtime allocation. P.P. and J.C.A.Q. acknowledge partial funding from the ANR (TRAPPER project) and the Colciencias (Q2DHOIP project) national research agencies. DFT calculations were done using French supercomputers (GENCI) through project 6194. This work was performed, in part, at the Center for Nanoscale Materials, a DOE Office of Science User Facility, and supported by the U.S. Department of Energy, Office of Science, Office of Basic Energy Sciences under Contract No. DE-AC02-06CH11357.

## Conflict of Interest

The authors declare no conflict of interest.

## Data Availability Statement

The data that support the findings of this study are available from the corresponding author upon reasonable request.

## Keywords

halide perovskites, microstructure, strain, synchrotron, texture, thin layers, X-ray diffraction

Received: November 18, 2021
Revised: February 7, 2022
Published online: February 26, 2022

[1] D. Liu, D. Luo, A. N. Iqbal, K. W. P. Orr, T. A. S. Doherty, Z.-H. Lu, S. D. Stranks, W. Zhang, *Nat. Mater.* **2021**, *20*, 1337.
[2] R. M. Kennard, C. J. Dahlman, R. A. DeCrescent, J. A. Schuller, K. Mukherjee, R. Seshadri, M. L. Chabinyc, *Chem. Mater.* **2021**, *33*, 298.
[3] J. Zhao, Y. Deng, H. Wei, X. Zheng, Z. Yu, Y. Shao, J. E. Shield, J. Huang, *Sci. Adv.* **2017**, *3*, eaao5616.
[4] D. B. Kim, J. W. Lee, Y. S. Cho, *Adv. Funct. Mater.* **2021**, *31*, 2007131.
[5] N. Rolston, K. A. Bush, A. D. Printz, A. Gold-Parker, Y. Ding, M. F. Toney, M. D. McGehee, R. H. Dauskardt, *Adv. Energy Mater.* **2018**, *8*, 1802139.
[6] D.-J. Xue, *Nat. Commun.* **2020**, *11*, 1514.
[7] Y. Jiao, S. Yi, H. Wang, B. Li, W. Hao, L. Pan, Y. Shi, X. Li, P. Liu, H. Zhang, C. Gao, J. Zhao, J. Lu, *Adv. Funct. Mater.* **2021**, *31*, 2006243.
[8] J. Feng, *APL Mater.* **2014**, *2*, 081801.
[9] A. C. Ferreira, A. Létoublon, S. Paofai, S. Raymond, C. Ecolivet, B. Rufflé, S. Cordier, C. Katan, M. I. Saidaminov, A. A. Zhumekenov, O. M. Bakr, J. Even, P. Bourges, *Phys. Rev. Lett.* **2018**, *121*, 085502.

[10] A. M. Lomonosov, X. Yan, C. Sheng, V. E. Gusev, C. Ni, Z. Shen, *Phys. Status Solidi RRL* **2016**, *10*, 606.
[11] N. Pandech, K. Sarasamak, S. Limpijumnong, *J. Appl. Phys.* **2015**, *117*, 174108.
[12] A. A. Medjahed, P. Dally, T. Zhou, N. Lemaitre, D. Djurado, P. Reiss, S. Pouget, *Chem. Mater.* **2020**, *32*, 3346.
[13] C. Stoumpos, C. D. Malliakas, M. G. Kanatzidis, *Inorg. Chem.* **2013**, *52*, 9019.
[14] E. C. Schueller, G. Laurita, D. H. Fabini, C. Stoumpos, M. G. Kanatzidis, R. Seshadri, *Inorg. Chem.* **2018**, *57*, 695.
[15] D. H. Fabini, R. Seshadri, M. G. Kanatzidis, *MRS Bull.* **2020**, *45*, 467.
[16] H. Mehdi, A. Mhamdi, A. Bouazizi, *Mater. Sci. Semicond. Process.* **2020**, *109*, 104915.
[17] S. T. Williams, F. Zuo, C.-C. Chueh, C.-Y. Liao, P.-W. Liang, A. K.-Y. Jen, *ACS Nano* **2014**, *8*, 10640.
[18] K. Zhang, Y. Zhao, R. Duan, P. Huang, K. Zhu, Z. Li, B. Dong, Y. Zhou, H. Zhu, B. Song, *Org. Electron.* **2019**, *68*, 96.
[19] Q. Wang, M. Lyu, M. Zhang, J.-H. Yun, H. Chen, L. Wang, *J. Phys. Chem. Lett.* **2015**, *6*, 4379.
[20] P.-A. Mante, C. Stoumpos, M. G. Kanatzidis, A. Yartsev, *J. Phys. Chem. Lett.* **2018**, *9*, 3161.
[21] P. Zhao, J. Su, Z. Lin, J. Wang, J. Zhang, Y. Hao, X. Ouyang, J. Chang, *Mater. Today Energy* **2020**, *17*, 100481.
[22] J. Ding, S. Du, X. Cheng, L. Jing, Y. Zhao, Z. Zuo, H. Cui, X. Zhan, *Mater. Chem. Phys.* **2018**, *204*, 222.
[23] M. U. Rothmann, W. Li, Y. Zhu, U. Bach, L. Spiccia, J. Etheridge, Y.-B. Cheng, *Nat. Commun.* **2017**, *8*, 14547.
[24] I. M. Hermes, S. A. Bretschneider, V. W. Bergmann, D. Li, A. Klasen, J. Mars, W. Tremel, F. Laquai, H.-J. Butt, M. Mezger, R. Berger, B. J. Rodriguez, S. A. L. Weber, *J. Phys. Chem. C* **2016**, *120*, 5724.
[25] Y. Liu, A. V. Ievlev, L. Collins, N. Borodinov, A. Belianinov, J. K. Keum, M. Wang, M. Ahmadi, S. Jesse, K. Xiao, B. G. Sumpter, B. Hu, S. V. Kalinin, O. S. Ovchinnikova, *Adv. Opt. Mater.* **2019**, *7*, 1901451.
[26] Y. Liu, P. Trimby, L. Collins, M. Ahmadi, A. Winkelmann, R. Proksch, O. S. Ovchinnikova, *ACS Nano* **2021**, *15*, 7139.
[27] P. S. Whitfield, N. Herron, W. E. Guise, K. Page, Y. Q. Cheng, I. Milas, M. K. Crawford, *Sci. Rep.* **2016**, *6*, 35685.
[28] K. Aizu, *J. Phys. Soc. Jpn.* **1969**, *27*, 1374B.
[29] E. Strelcov, Q. Dong, T. Li, J. Chae, Y. Shao, Y. Deng, A. Gruverman, J. Huang, A. Centrone, *Sci. Adv.* **2017**, *3*, e1602165.
[30] J. Breternitz, M. Tovar, S. Schorr, *Sci. Rep.* **2020**, *10*, 16613.
[31] B. Saparov, D. B. Mitzi, *Chem. Rev.* **2016**, *116*, 4558.
[32] K. Wang, D. Yang, C. Wu, M. Sanghadasa, S. Priya, *Prog. Mater. Sci.* **2019**, *106*, 100580.
[33] A. Franz, D. M. Többens, J. Steckhan, S. Schorr, *Acta Crystallogr. B* **2018**, *74*, 445.
[34] S. Colella, E. Mosconi, G. Pellegrino, A. Alberti, V. L. P. Guerra, S. Masi, A. Listorti, A. Rizzo, G. G. Condorelli, F. De Angelis, G. Gigli, *J. Phys. Chem. Lett.* **2014**, *5*, 3532.
[35] S. D. Stranks, G. E. Eperon, G. Grancini, C. Menelaou, M. J. P. Alcocer, T. Leijtens, L. M. Herz, A. Petrozza, H. J. Snaith, *Science* **2013**, *342*, 341.
[36] W. A. Dunlap-Shohl, Y. Zhou, N. P. Padture, D. B. Mitzi, *Chem. Rev.* **2019**, *119*, 3193.
[37] M. Bouchard, J. Hilhorst, S. Pouget, F. Alam, M. Mendez, D. Djurado, D. Aldakov, T. Schülli, P. Reiss, *J. Phys. Chem. C* **2017**, *121*, 7596.
[38] Y. Zhou, O. S. Game, S. Pang, N. P. Padture, *J. Phys. Chem. Lett.* **2015**, *6*, 4827.
[39] T. J. Jacobsson, L. J. Schwan, M. Ottosson, A. Hagfeldt, T. Edvinsson, *Inorg. Chem.* **2015**, *54*, 10678.
[40] C. Ge, M. Hu, P. Wu, Q. Tan, Z. Chen, Y. Wang, J. Shi, J. Feng, *J. Phys. Chem. C* **2018**, *122*, 15973.
[41] J. W. Matthews, A. E. Blakeslee, *J. Cryst. Growth* **1974**, *27*, 118.
[42] A. Gangulee, *Acta Metall.* **1974**, *22*, 177.
[43] M. U. Rothmann, J. S. Kim, J. Borchert, K. B. Lohmann, C. M. O'Leary, A. A. Sheader, L. Clark, H. J. Snaith, M. B. Johnston, P. D. Nellist, L. M. Herz, *Science* **2020**, *370*, eabb5940.
[44] M. Xiao, F. Huang, W. Huang, Y. Dkhissi, Y. Zhu, J. Etheridge, A. Gray-Weale, U. Bach, Y.-B. Cheng, L. Spiccia, *Angew. Chem.* **2014**, *126*, 10056.
[45] N. J. Jeon, J. H. Noh, Y. C. Kim, W. S. Yang, S. Ryu, S. Seok, *Nat. Mater.* **2014**, *13*, 897.
[46] Y. Zhou, H. Zhou, J. Deng, W. Cha, Z. Cai, *Matter* **2020**, *2*, 360.
[47] J. Hilhorst, F. Marschall, T. N. Tran Thi, A. Last, T. U. Schülli, *J. App. Cryst.* **2014**, *47*, 1882.
[48] S. J. Leake, G. A. Chahine, H. Djazouli, T. Zhou, C. Richter, J. Hilhorst, L. Petit, M.-I. Richard, C. Morawe, R. Barrett, L. Zhang, R. A. Homs-Regojo, V. Favre-Nicolin, P. Boesecke, T. Schülli, *J. Synchrotron Rad.* **2019**, *26*, 571.
[49] T. Zhou, T. Stankevic, A. Troian, Z. Ren, Z. Bi, J. Ohlsson, L. Samuelson, J. Hilhorst, T. Schulli, A. Mikkelsen, O. Balmes, *Microsc. Microanal.* **2018**, *24*, 128.
[50] J.-C. Toledano, *Ann. Télécommun.* **1974**, *29*, 249.
[51] J. D. McGettrick, K. Hooper, A. Pockett, J. Baker, J. Troughton, M. Carnie, T. Watson, *Mater. Lett.* **2019**, *251*, 98.
[52] S. Svanström, A. G. Fernández, T. Sloboda, T. Jesper Jacobsson, H. Rensmo, U. B. Cappel, *Phys. Chem. Chem. Phys.* **2021**, *23*, 12479.
[53] M. E. Stuckelberger, T. Nietzold, B. M. West, Y. Luo, X. Li, J. Werner, B. Niesen, C. Ballif, V. Rose, D. P. Fenning, M. I. Bertoni, *J. Phys. Chem. C* **2020**, *124*, 17949.
[54] J. P. Perdew, K. Burke, M. Ernzerhof, *Phys. Rev. Lett.* **1996**, *77*, 3865.
[55] G. Kresse, J. Furthmüller, *Phys. Rev. B* **1996**, *54*, 11169.
[56] P. E. Blöchl, *Phys. Rev. B* **1994**, *50*, 17953.